Original Article

# Sustained BMP-2 delivery via alginate microbeads and polydopamine-coated 3D-Printed PCL/β-TCP scaffold enhances bone regeneration in long bone segmental defects

Seoyun Lee [a,b], Jae-Hun Kim [c], Yong-Hun Kim [d], Jihyeock Hong [e], Woo Keyoung Kim [a,b], Songwan Jin [d,e], Byung-Jae Kang [a,b,*]

[a] Department of Veterinary Clinical Sciences, College of Veterinary Medicine and Research Institute for Veterinary Science, Seoul National University, Seoul, 08826, South Korea
[b] BK21 FOUR Future Veterinary Medicine Leading Education and Research Center, Seoul National University, Seoul, 08826, South Korea
[c] Department of Mechanical System Engineering, Graduate School of Knowledge-based Technology and Energy, Tech University of Korea, Gyeonggi, 15073, South Korea
[d] T&R Biofab Co. Ltd., Gyeonggi, 15073, South Korea
[e] Department of Mechanical Engineering, Tech University of Korea, Gyeonggi, 15073, South Korea

## ARTICLE INFO

## ABSTRACT

*Background/Objective:* Repair of long bone defects remains a major challenge in clinical practice, necessitating the use of bone grafts, growth factors, and mechanical stability. Hence, a combination therapy involving a 3D-printed polycaprolactone (PCL)/β-tricalcium phosphate (β-TCP) scaffold coated with polydopamine (PDA) and alginate microbeads (AM) for sustained delivery of bone morphogenetic protein-2 (BMP-2) was investigated to treat long bone segmental defects.

*Methods:* Several in vitro analyses were performed to evaluate the scaffold osteogenic effects in vitro such as PDA surface modification, namely, hydrophilicity and cell adhesion; cytotoxicity and BMP-2 release kinetics using CCK-8 assay and ELISA, respectively; osteogenic differentiation in canine adipose-derived mesenchymal stem cells (Ad-MSCs); formation of mineralized nodules using ALP staining and ARS staining; and mRNA expression of osteogenic differentiation markers using RT-qPCR. Bone regeneration in femoral bone defects was evaluated in vivo using a rabbit femoral segmental bone defect model by performing radiography, micro-computed tomography, and histological observation (hematoxylin and eosin and Masson's trichrome staining).

*Results:* The PDA-coated 3D-printed scaffold demonstrated increased hydrophilicity, cell adhesion, and cell proliferation compared with that of the control. BMP-2 release kinetics assessment showed that BMP-2 AM showed a reduced initial burst and continuous release for 28 days. *In vitro* co-culture with canine Ad-MSCs showed an increase in mineralization and mRNA expression of osteogenic markers in the BMP-2 AM group compared with that of the BMP-2-adsorbed scaffold group. *In vivo* bone regeneration evaluation 12 weeks after surgery showed that the BMP-2 AM/PDA group exhibited the highest bone volume in the scaffold, followed by the BMP-2/PDA group. High cortical bone connectivity was observed in the PDA-coated scaffold groups.

*Conclusion:* These findings suggest that the combined use of PDA-coated 3D-printed bone scaffolds and BMP-2 AM can successfully induce bone regeneration even in load-bearing bone segmental defects.

*The translational potential of this article:* A 3D-printed PCL/β-TCP scaffold was fabricated to mimic the cortical bone of the femur. Along with the application of PDA surface modification and sustained BMP-2 release via AM, the developed scaffold could provide suitable osteoconduction, osteoinduction, and osteogenesis in both in vitro settings and in vivo rabbit femoral segmental bone defect models. Therefore, our findings suggest a promising therapeutic option for treating challenging long bone segmental defects, with potential for future clinical application.

---

\* Corresponding author. Department of Veterinary Clinical Sciences, College of Veterinary Medicine, Seoul National University, Seoul, 08826, South Korea.
E-mail address: bjkang81@snu.ac.kr (B.-J. Kang).

# 1. Introduction

The complicated biology and biomechanics underlying the bone healing process remain a subject of ongoing investigation in scientific research. Long bones, such as the tibia and femur, are weight-bearing bones that provide mechanical stability. Therefore, the surgical treatment of long bone segmental critical-sized defects due to factors such as fractures, infections, or congenital abnormalities is challenging because, in addition to bone regeneration, mechanical support also needs to be addressed [1]. Traditionally, vascularized bone grafts harvested from the iliac crest, rib, or fibula have been the preferred method for managing such defects. However, these techniques have limitations such as donor site morbidity, infection, pain, and potential disparities in bone graft size [2]. Alternative approaches, such as distraction osteogenesis using the Ilizarov and Masquelet techniques, have been employed; however, they require a subsequent surgical procedure and long recovery periods, thereby increasing the risk of infection [3,4]. Therefore, tissue-engineering strategies utilizing bioactive scaffolds and growth factors have emerged as promising alternatives for bone regeneration with the potential to overcome the limitations associated with traditional treatment methods [5].

Among the various strategies for tissue engineering, the use of three-dimensional (3D)-printed scaffolds has gained significant attention because of their ability to replicate the complex architecture of native bone tissue [6]. Polycaprolactone (PCL) and beta-tricalcium phosphate ($\beta$-TCP) are biocompatible and biodegradable materials frequently used in bone tissue engineering to fabricate 3D-printed scaffolds. PCL is a thermoplastic polymer that offers high processability for printing complex shapes and exhibits favourable mechanical strength with slow in vivo degradation. Conversely, the hydrophobic characteristic of PCL surfaces hinders effective cell adhesion and viability [7]. In contrast, $\beta$-TCP is a bio-ceramic material with a mineral composition that resembles natural bone and possesses remarkable osteoconductivity as it promotes mineralization through the local release of calcium ions during degradation. However, it has limitations in terms of mechanical strength and rapid absorption in the body, which restricts its use in bone-defect regeneration [8]. Therefore, incorporating both PCL and $\beta$-TCP into the scaffold design can overcome the individual drawbacks of each material, leading to enhanced mechanical support and osteoconduction in load-bearing applications [9]. Nonetheless, achieving sufficient osteoinduction and osteogenesis solely using a 3D scaffold remains challenging because of the lack of inherent bioactivity.

Therefore, current research primarily focuses on enhancing the osseointegration of 3D-printed scaffolds through various approaches, such as surface modifications to improve cell adhesion or the simultaneous administration of bioactive growth factors [10]. Polydopamine (PDA) is a mussel-inspired polymer that is preferred for application in these techniques because of its strong adhesive nature on diverse material surfaces, including superhydrophobic surfaces [11]. PDA usage is a simple and effective method for surface modification that involves an oxidative reaction between dopamine and oxygen under alkaline conditions. The high proportion of catechol and amine functional groups in the PDA coating increases the hydrophilicity of the surface and the attachment of growth factors and cells, promoting their interaction with the scaffold surface and facilitating cell proliferation [12–14]. Although previous studies have demonstrated the ability of PDA-coated hydroxyapatite [15], poly lactic-*co*-glycolic acid [16], and Ti6Al4V [17] scaffolds to enhance new bone formation in bone defect models, the potential of PCL/$\beta$-TCP scaffolds remains unexplored.

Moreover, the combination of 3D-printed scaffolds with growth factors such as bone morphogenetic protein-2 (BMP-2) is a widely adopted strategy for enhancing scaffold bioactivity and accelerating bone regeneration [18]. BMP-2 plays a crucial role in the initial stages of bone regeneration by promoting the recruitment and differentiation of mesenchymal stem cells (MSCs). However, the rapid release and short half-life of BMP-2 can limit its efficacy, often requiring high doses that

may lead to undesirable effects including cystic bone formation and heterotopic ossification [19,20]. To overcome these limitations, sustained-release delivery systems for BMP-2 have been developed such as the use of alginate, which is a biocompatible natural polysaccharide derived from brown algae. Alginate possesses favourable properties as a scaffold material and enables the encapsulation of bioactive molecules via cross-linking reactions [21]. Previous studies using BMP-2-loaded alginate microbeads (AM) have demonstrated the sustained release of BMP-2 over a period of 28 days, which effectively stimulated bone growth in experimental models of calvarial and metaphyseal bone defects [22,23]. Hence, integrating BMP-2 loaded AM into 3D-printed scaffolds would enable precise spatiotemporal control over the release of BMP-2 and optimise its therapeutic effects.

In this study, a 3D-printed PCL/$\beta$-TCP scaffold that mimics the cortical structure of long bones was developed. Next, the release kinetics of growth factors, cell attachment capability, and osteogenic potential of scaffolds incorporated with adsorbing BMP-2 and concurrent application of BMP-2 AM were examined. Additionally, the in vivo bone regeneration and osseointegration within the scaffold were analysed using a rabbit femoral diaphyseal bone defect model. Ultimately, the objective of this research is to demonstrate that combining the 3D-printed PCL/$\beta$-TCP scaffold with BMP-2 delivered via alginate microbeads offers a feasible and effective clinical strategy for addressing load-bearing bone defects.

# 2. Materials & methods

## 2.1. Preparation, morphology, and encapsulation efficiency of BMP-2 alginate microbeads

Sodium alginate powder (80–120 cP; Wako, Osaka, Japan) was sterilized using a hydrogen peroxide gas plasma treatment before use. A 2.0 % sodium alginate solution was prepared by dissolving 2 g of the powder in 100 mL of distilled water (DW). To produce BMP-2-containing microbeads, 500 μg of BMP-2 (Novosis, CGbio Inc., Seongnam, Korea) was diluted in 0.8 mL of DW and combined with 1.2 mL of the 2.0 % sodium alginate solution. BMP-2-loaded microbeads were manufactured using an encapsulator (B-395 Pro; Büchi Labortechnik AG, Flawil, Switzerland) with the following modified parameters based on a previous experiment [23]: nozzle diameter: 120 μm, frequency: 1000 Hz, electrode potential: 600 V, stirring rate: 80 %, and flow rate: 1.6 mL/min. After gelation for 30 min in a 250 mL CaCl$_2$ solution, the microbeads were washed twice with DW and prepared for use.

To assess the surface characteristics and internal structure of alginate microbeads, cryo-field emission scanning electron microscopy (Cryo-FESEM, Crossbeam 550; Carl Zeiss, Oberkochen, Germany) was employed. The bead samples were affixed to an aluminum holder and immersed into a liquid nitrogen slush at −210 °C. After being frozen, they were transferred to a cryo-preparation chamber and fractured at −140 °C. The samples were subsequently etched at −90 °C for 30 min, coated with platinum, and observed under an accelerating voltage of 5 kV.

The fabricated beads were dissolved in a 2 % w/v sodium citrate solution (Sigma–Aldrich, Steinheim, Germany) and stored at −80 °C. Subsequently, an enzyme-linked immunosorbent assay (ELISA) (DBP200; R&D Systems, Minneapolis, MN, USA) was performed to quantify the concentration of BMP-2 encapsulated in AM, following the manufacturer's instructions. The encapsulation efficiency (EE) of AM was calculated using the following formula: Encapsulation efficiency = ((amount of BMP-2 in dissolved AM)/(total amount of loaded BMP-2)) × 100.

## 2.2. Design and fabrication of 3D-printed PCL/$\beta$-TCP scaffolds

The scaffold used in this study had a thick, cylindrical shape and was designed by referring to the cortical bone and medullary cavity

structures found in rabbit femurs. The 3D printing path was designed in a continuous line-drawing manner to prevent oozing and stringing. PCL (26288, Polyscience Inc., Warrington, PA, USA) and β-TCP (Foster Corporation, Putnam, CT, USA) were used to fabricate the scaffolds. To blend PCL with β-TCP, 0.8 g of PCL was melted on a hot plate at 140 °C, to which 0.2 g of β-TCP was added. The molten PCL and β-TCP were mixed using a sharp tool until they were homogeneously blended and placed into a stainless-steel syringe. The PCL/β-TCP scaffolds were fabricated using a commercialized 3D bioprinting system (3DX printer; T&R Biofab Co., Ltd., Siheung, Korea) that had a nozzle diameter of 500 μm. The working temperature and pressure were 120 °C and 500 kPa, respectively.

### 2.3. Polydopamine surface coating and evaluation of hydrophilicity and cell adhesion on 3D-Printed implants

For surface modification with the PDA coating, a 1 or 2 mg/mL dopamine hydrochloride (Sigma–Aldrich) solution was prepared in 10 mM Tris–HCl buffer (pH 8.5; T&I, Chuncheon, Korea) and incubated overnight at room temperature (RT) on a 25 rpm shaker in the dark. Following implant fabrication, the 3D-printed implants were washed with deionized water, immersed in the prepared dopamine solution, and incubated overnight under the same conditions. Then, all scaffolds were rinsed with deionized water and air-dried under UV light before use. The hydrophilicity was evaluated by measuring the water contact angle with 2 μl of deionized water on the immobilized implant and calculating the angle between the surface of the implant and the point of contact with the water droplets using ImageJ software (NIH, Bethesda, MD, USA). To assess cell adhesion, $1 \times 10^5$ canine Ad-MSCs expressing green fluorescent protein were seeded into the scaffolds with 1.5 mL of cell culture media, comprising DMEM, 10 % fetal bovine serum (FBS), and 1 % penicillin-streptomycin (PS). The scaffolds were incubated in a 24-well plate for 1 h at 37 °C to induce cell adhesion. Following this, 1 mL of fresh cell culture media was added to each well, and the scaffolds were incubated at 37 °C with 5 % $CO_2$ for 15 days; the media was replaced every 2 days. The extent of cell adhesion was observed using fluorescence microscopy, and the cell adhesion ratio was quantified using ImageJ software (NIH). To examine cell attachment and spreading on 3D-printed scaffolds after a 3-day co-culture with canine Ad-MSCs, field emission scanning electron microscopy (FESEM) was utilized. Following fixation and dehydration pretreatment, the samples were dried with hexamethyldisilazane for 20 min. The scaffolds were then mounted on aluminum stubs with copper conductive tape and further dried in a vacuum desiccator for 3 days. After being coated with platinum for 120 s at 30 mA, the samples were examined using a FESEM instrument (SIGMA; Carl Zeiss) operated at 5 kV.

### 2.4. In vitro cytotoxicity and BMP-2 release profiles from alginate microbeads and 3D-printed scaffolds

*In vitro* cytotoxicity assessment was conducted using the Cell Counting Kit-8 (CCK-8; Dojindo, Kumamoto, Japan) to evaluate the potential cytotoxic effects of the alginate microbeads and 3D-printed scaffolds. Canine Ad-MSCs were seeded at a density of $2 \times 10^4$ cells/well in a 12-well plate and allowed to adhere for 1 day at 37 °C with 5 % $CO_2$. The culture medium was then replaced with fresh media, and the cells were co-cultured with each implant using 0.4 μm SPLInsert™ Hanging (SPL Life Bioscience, Pocheon, Korea). After co-culturing for 24, 48, and 72 h, the cells were treated with CCK-8 solution (100 L/well) and incubated for 1 h. The cell viability was assessed by measuring the absorbance at 450 nm. *In vitro* release kinetics of BMP-2 from both the AM- and 3D-printed scaffolds were determined using a BMP-2 Quantikine ELISA Kit (R&D Systems) to examine the effectiveness of the implants as delivery carriers. The release patterns and abilities of each implant were investigated, including BMP-2 adsorbed scaffold, BMP-2-adsorbed PDA-coated scaffold (BMP-2/PDA), BMP-2 AM with a non-coated scaffold (BMP-2 AM), and BMP-2 AM with a PDA-coated scaffold (BMP-2 AM/PDA). These implants were placed on a hanging insert in a 6-well plate (SPL Life Bioscience) and immersed in a 4 mL release medium consisting of phenol red-free DMEM, 10 % FBS, and 1 % PS for 28 days at RT under mild shaking at 70 rpm. The samples were collected and kept at −80 °C and used for ELISA analysis after 1, 3, 5, 7, 14, 21, and 28 days of incubation; the release medium was replaced each time.

### 2.5. Osteogenic differentiation of canine adipose-derived mesenchymal stem cells co-cultured with implants

*In vitro* osteoinductive potency of the implants was assessed by coculturing canine Ad-MSCs with the implants and evaluating their osteogenic differentiation. Canine Ad-MSCs were seeded onto a 6-well culture plate at a density of $1 \times 10^4$ cells/cm$^2$ and allowed to attach for 24 h at 37 °C with 5 % $CO_2$. Subsequently, the cell culture medium was removed, and the cells were washed twice with Dulbecco's phosphate-buffered saline (DPBS). Then, 4 mL of osteogenic differentiation medium composed of DMEM, 10 % FBS, 1 % PS, 50 μg/mL ascorbic acid 2-phophate (Sigma–Aldrich), 100 nM dexamethasone (Sigma–Aldrich), and 10 mM β-glycerophosphate (Sigma–Aldrich) were added. Hanging inserts (SPL Life Biosciences) containing individual implants, BMP-2-adsorbed scaffolds, BMP-2-adsorbed PDA-coated scaffolds, and BMP-2 AM were placed in each well, and a control was established using only the upper insert. The cells were incubated for 7 or 14 days, and the osteogenic medium was gently replaced twice a week after the cells were carefully washed once each time.

### 2.6. Alkaline phosphatase staining

Alkaline phosphatase (ALP) staining was performed to evaluate ALP activity after the induction of osteogenic differentiation for 7 and 14 days. After removal of the osteogenic medium, the cells were rinsed twice with PBS, fixed with 4 % paraformaldehyde for 2 min, and washed with PBS. Thereafter, a BCIP/NCT substrate solution (250 μL/cm$^2$; Sigma–Aldrich) was added to each well and incubated at RT for 4 h. The wells were washed with PBS to eliminate the substrate solution, immersed in 1 mL of DW, and observed under an optical microscope. The ALP-stained area ratio was analysed using ImageJ software (NIH).

### 2.7. Alizarin Red S staining

Alizarin Red S (ARS) staining was performed to observe the formation of mineralized nodules after 14 days. The cell culture medium was removed and washed twice with DPBS before being fixed with 4 % paraformaldehyde at RT for 10 min. After washing thrice with DW, 0.5 mL of 40 mM ARS solution (pH 4.3; Sigma–Aldrich) was added to each well and incubated at RT for 20 min in the dark. The staining solution was then removed. The wells were washed five times with DW, and 1 mL of DPBS was added to observe the calcium nodules using optical microscopy. To determine the extent of mineralization, the stained wells were treated with 2 mL of 10 % cetylpyridinium chloride (Sigma–Aldrich) and incubated at RT for 15 min with shaking at 100 rpm. Afterwards, 100 μL of solutions were transferred to a 96-well plate, and the absorbance was measured at 570 nm.

### 2.8. Real time quantitative PCR

The mRNA expression of the osteogenic differentiation markers was investigated using RT-qPCR on days 7 and 14. Total RNA was extracted from cultured cells using the QIAzol® Lysis Reagent (Qiagen, Valencia, CA, USA) following the manufacturer's instructions. The RNA concentration was determined using an Epoch Take3 microvolume spectrophotometer (BioTek, Winooski, VT, USA). cDNA was synthesized using the PrimeScript™ II 1st strand cDNA Synthesis Kit (Takara, Shiga, Japan) with 2 μg of total RNA. Gene expression was quantitated using

the StepOnePlus™ Real-Time PCR System (Applied Biosystems, Waltham, MA, USA) with TB Green™ Premix Ex Taq™ II (Takara) and gene-specific primers. The following primer sequences were used: GAPDH, 5′-TGC CCA GAA CAT CAT CCC TG-3′ and 5′-TCC GAT GCC TGC TTC ACT AC-3′; COL1A1, 5′-CCT GGC AAG AAC GGA GAT GA-3′ and 5′-TCC ATT TTC ACC GGG GCT AC-3′; ALP, 5′-GCT TGT TTC TCT GGG AAG AGC-3′ and 5′-CCC AGA GGC ATT CTG TTG GAT-3′. The mRNA expression levels of osteogenic marker genes were calculated using the $2^{-\Delta\Delta Ct}$ method, normalized to the GAPDH gene, and presented as fold change relative to the negative control.

### 2.9. In vivo bone regeneration in a rabbit femoral segmental defect model

In total, 20 male New Zealand White rabbits weighing 3.0–3.5 kg were included in this study to investigate the bone regeneration potential in vivo. The rabbits were acclimatized to their diet, housing, and water for 2 weeks before the surgical intervention was administered. All animals were divided into five groups of four as follows: 1) Scaffold (control) group; 2) BMP-2 scaffold (BMP-2) group (n = 4); 3) BMP-2 alginate microbeads/scaffold (BMP-2 AM) group (n = 4); 4) BMP-2/PDA-coated scaffold (BMP-2/PDA) group (n = 4); and 5) BMP-2 alginate microbeads/PDA-coated scaffold (BMP-2 AM/PDA) group (n = 4). Prior to the surgical procedure, the rabbits were sedated with an intramuscular injection of medetomidine (0.3 mg/kg, Domitor®; Zoetis, Seoul, Korea). Antibiotics and analgesics were administered subcutaneously. Anaesthesia was induced with 4–5 minimum alveolar concentrations (MAC) of isoflurane at 1–2 L/min of $O_2$ and maintained at 1.5–2 MAC with the same $O_2$ flow rate throughout the surgery. Following extensive hair clipping of the right hind limb, the surgical site was thoroughly disinfected using a chlorhexidine-alcohol solution and draped. A skin incision was made from the greater trochanter to the lateral condyle of the right femur in the left lateral recumbent position. The fascia lata between the vastus lateralis and biceps femoris was incised, and the muscles were retracted to expose the femoral diaphysis. Before inflicting the bone defect, a 12-hole 1.5/2.0 mm locking plate (Jeil Medical Corp., Seoul, Korea) was placed in the craniolateral direction, and a screw hole was made in advance to prevent rotation. After removing the plate, a 12 mm defect was formed perpendicular to the bone axis using an oscillating saw (Colibri II; Depuy Synthes, Oberdorf, Switzerland) with continuous saline irrigation to avoid thermal injury. Subsequently, the scaffold, prepared according to the respective groups, was implanted at the bone defect site. The proximal and distal femur and the scaffold were secured with the plate and bone screws. Afterwards, an 8-hole 1.2 mm locking plate (Jeil Medical) was applied in the caudomedial direction for orthogonal plating. Muscle and subcutaneous tissues were sutured using 3-0 polydioxanone suture material and the skin was closed with a 3-0 nylon monofilament suture. To minimize the risk of postoperative complications, the surgical site was disinfected, and antibiotics and analgesics were administered subcutaneously for 7 days. All animal experimental procedures were approved by the Institutional Animal Care and Use Committee of the affiliated institution.

### 2.10. Radiographic and micro-CT analysis

Radiographic images were obtained at 4, 8, and 12-week post-surgery to monitor bone repair serially. All X-ray images were scored between 0 and 10 based on the pre-existing radiological scoring system for bone defect recovery (Supplementary Table 1). After 12 weeks, the rabbits were deeply anesthetized with 5 MAC isoflurane and euthanized using an intravenous bolus injection of 150 mg/kg KCl solution. The femur was harvested, the soft tissue surrounding the bony tissue was trimmed, and the bone plates and screws were removed. After 2 days of fixation with 10 % neutral buffered formalin, the samples were rinsed in PBS for 1 day at 4 °C prior to micro-CT scanning, which was performed using a Quantum GX2 system (Perkin Elmer, Waltham, MA, USA) at the following settings: voltage of 90 kV, current of 88 µA, acquisition field of

view of 72 mm, voxel size of 90 µm, high-resolution scan mode, and X-ray filter of 0.06 mm Cu and 0.5 mm Al. The resulting images were reconstructed using 3D viewer software (version 6.1.7; Perkin Elmer) and analysed using CTan software (Bruker, Kontich, Belgium). To quantify the amount of bone formation inside and outside the scaffold, two regions of interest (ROI) were defined for measurement: the scaffold ROI and the peripheral ROI. Afterwards, bone volume (BV) and polar moment of inertia (pMOI) were calculated.

### 2.11. Histological analyses

Following micro-CT analysis, the fixed samples were decalcified in 10 % ethylenediamine tetraacetic acid (EDTA) solution (National Diagnostics, Atlanta, GA, USA) at RT for 1 month and embedded in paraffin. Sagittal sections (5 µm thick) were obtained and stained with hematoxylin and eosin (H&E) and Masson's trichrome (Abcam, Cambridge, UK).

### 2.12. Statistical analysis

Quantitative data are presented as mean ± standard deviation (SD), and statistical analyses were performed using GraphPad Prism (version 8.0.1). Kruskal–Wallis and Mann–Whitney tests were used to determine the statistical significance between groups. p-values less than 0.05 ($p < 0.05$) were regarded as significant.

## 3. Results

### 3.1. Microscopic morphology, surface characteristics, and EE of alginate microbeads

The BMP-2-encapsulated AM was spherical and measured 275.9 ± 27.18 µm in diameter. Approximately 80 % of the produced beads had diameters ranging from 250 to 310 µm. Cryo-SEM images confirmed that the microbeads maintained a spherical shape with a rough surface texture. Cross-sectional analysis revealed a prominent porous architecture, suggesting its potential to enhance drug encapsulation and prolonged release (Fig. 1). ELISA measurements of BMP-2 quantity in dissolved microbeads showed that the EE of BMP-2-loaded AM was 63.10 ± 1.18 %, which is consistent with the results of previous experiments [23].

### 3.2. Structural properties of 3D-printed PCL/β-TCP scaffolds

The shapes of the scaffolds for transplantation onto the femoral bone defects were determined using CT images of the rabbit femur (Fig. 2A and B). The fabricated PCL/β-TCP scaffold was a white cylindrical structure with a 12-mm height and an oval-shaped cross-section (9 mm on the long axis and 8 mm on the short axis). The exterior surface of the scaffold was covered with a solid structure, whereas the interior structure was designed with star- and rectangle-shaped cross-sections to generate a crossing strand pattern, thereby facilitating the growth of the cortical bone (Fig. 2C and D). Each strand had a width of approximately 380 µm, and the distance between the stacked strands was approximately 150 µm.

### 3.3. Surface hydrophilicity and cell adhesion ability of scaffolds after PDA coating

Coating with PDA imparted a grey colour to the scaffold, which became greyer as the PDA concentration increased. Examination of the surface wettability and cell-adhesion capabilities of the 3D-printed scaffolds showed that the contact angle with water, which decreased as hydrophilicity increased, was lower in the PDA-coated groups than in the uncoated group. The control group had the highest contact angle of 84.52 ± 1.18°, whereas the contact angles for the PDA1 and PDA2
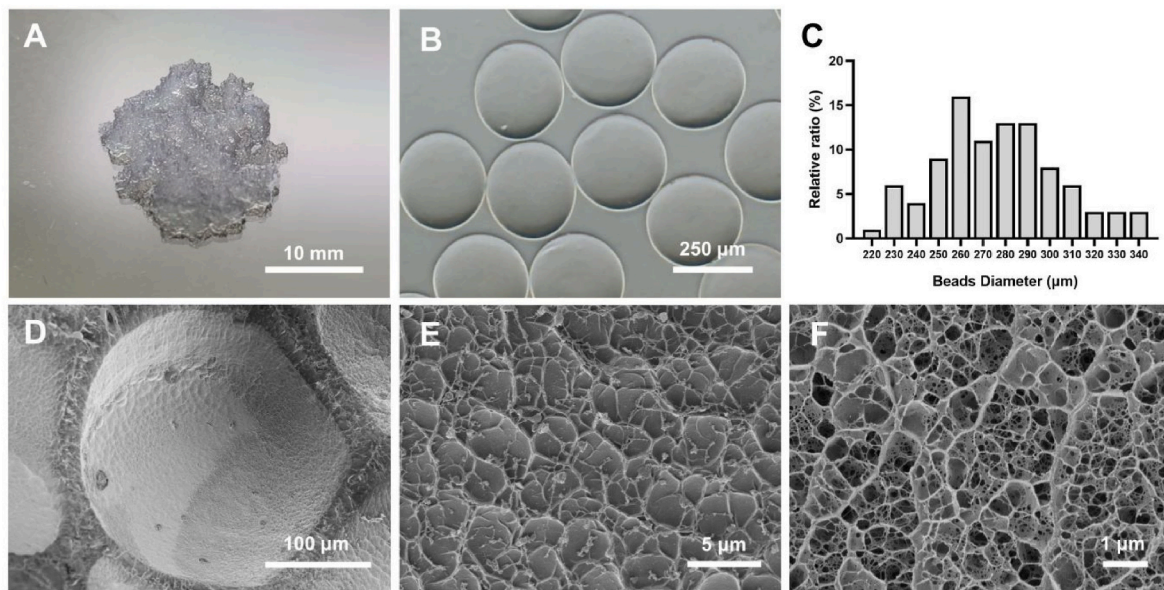
**Fig. 1. Morphology and size distribution analysis of fabricated alginate microbeads** (A) Gross morphology of produced alginate microbeads. Scale bar = 10 mm (B) Spherical shape observed under optical microscopy. Scale bar = 250 μm (C) Histogram indicating the distribution of the beads diameter (D–F) Cryo-FESEM images showed the magnified morphology, surface roughness, and cross section of the beads. Scale bar = 100 μm, 5 μm, and 1 μm, respectively.
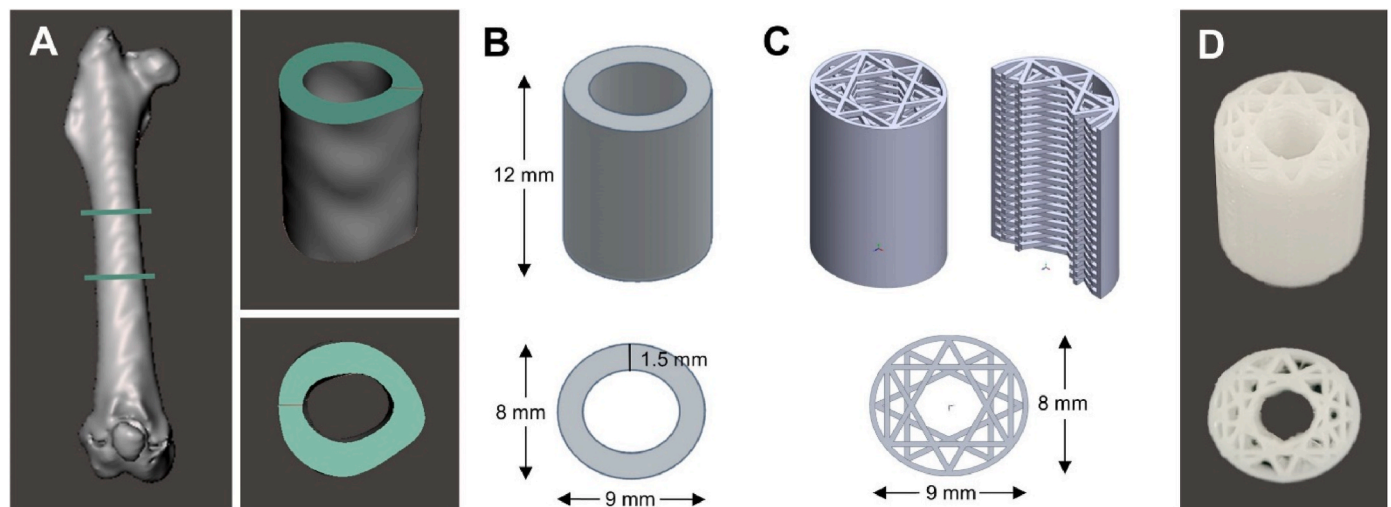


**Fig. 2. Design process and shape of 3D-printed scaffolds for rabbit femoral defects** (A and B) Using the computed tomographic image, the rabbit femur was reconstructed in 3D, and the cortical bone in the middle was extracted and reshaped to have a simplified shape (C) The structure was modified to facilitate 3D printing and bone ingrowth, and the scaffold was manufactured by stacking cross-sections of star and rectangle shapes within an oval (D) The final form of the 3D-printed scaffolds had a white cylindrical structure with a solid outer layer and a crossing strand pattern in the cortical bone region.

groups were $64.96 \pm 1.16°$ and $38.14 \pm 1.80°$, respectively ($p < 0.01$) (Fig. 3A). Furthermore, the cell adhesion ratio was significantly higher in the PDA2 group on days 7 and 15, followed by that of the PDA1 and uncoated groups ($p < 0.01$). On day 15, the percentage of cell adhesion was found to be $4.85 \pm 0.35$ % for the control group, $15.42 \pm 1.15$ % for the PDA1 group, and $23.30 \pm 1.62$ % for the PDA2 group. Thus, the PDA2 group demonstrated a 4.8-fold increase in cell adhesion compared with that of the control group and a 1.5-fold increase compared with that of the PDA1 group (Fig. 3B and C). FESEM images provided detailed observations of cell–scaffold interactions. While cells were found to adhere to the implant surfaces irrespective of coating, scaffolds with PDA coating demonstrated a greater extent of cell attachment and coverage, reflecting enhanced cell spreading and more stable adhesion (Fig. 3D).

### 3.4. In vitro cytotoxicity for canine Ad-MSCs and BMP-2 release profiles of AM and 3D-printed scaffolds

The potential cytotoxicity of both AM- and 3D-printed scaffolds was evaluated by analysing the proliferation of canine Ad-MSCs co-cultured with implants not containing BMP-2. No significant differences were observed in cell proliferation among the control (insert only), AM-, and PDA-coated or non-coated 3D scaffold groups at 24, 48, and 72 h of co-culture (Fig. 4A). The release of BMP-2 was monitored for 28 days to assess the function of the implants as delivery carriers. In the BMP-2-adsorbed uncoated scaffold group, the highest initial burst was observed on the first day, with $62.27 \pm 0.87$ % of the loaded amount released. Afterwards, a plateau pattern was observed, with a release of $72.39 \pm 0.90$ % up to day 7 and $75.44 \pm 1.06$ % up to day 28. All groups incorporating BMP-2 AM scaffold exhibited a more gradual release
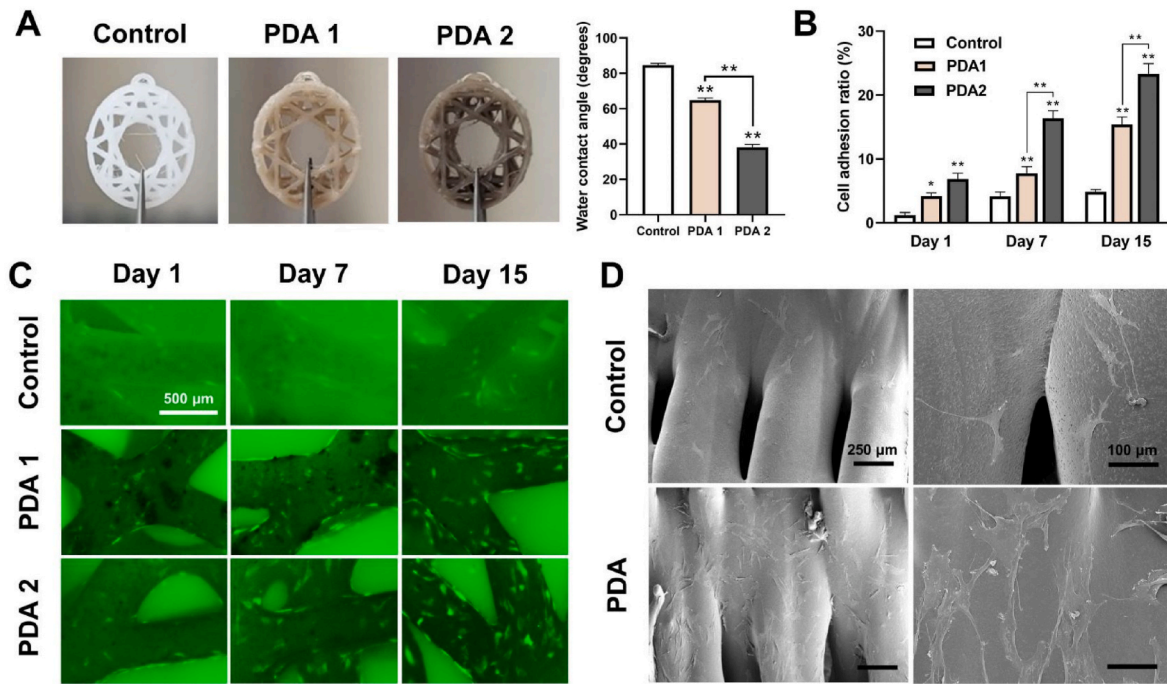
**Fig. 3. Surface modification of 3D-printed scaffolds after polydopamine coating.** The surface coating of implants was treated with either 1 mg/mL (PDA1) or 2 mg/mL (PDA2) of polydopamine (A) The hydrophilicity of the implant was assessed by placing 2 µL of deionized water on its surface and measuring the water contact angle (B and C) The cell adhesion ability was evaluated by co-culturing GFP-expressing cells and observing attached cells under fluorescence microscopy at days 1, 7, and 15. The cell adhesion ratio was calculated, and statistical significance was indicated by asterisks (*$p < 0.05$ and **$p < 0.01$). Scale bar = 500 µm (D) FESEM images of scaffolds with or without PDA coating at days 3. Scale bar = 250 µm and 100 µm.
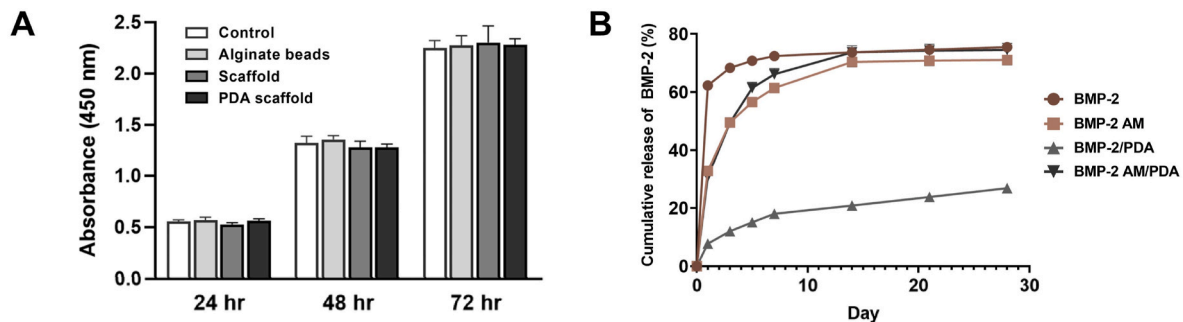


**Fig. 4. In vitro cytotoxicity and BMP-2 release pattern of implants** (A) The viability of canine Ad-MSCs was evaluated through a CCK-8 assay at 24, 48, and 72 h after co-culturing with different samples: only the upper insert (control), alginate microbeads, 3D-printed scaffold (scaffold), and PDA-coated scaffold (PDA scaffold). Additionally, (B) the release kinetics of BMP-2 from various scaffold materials, namely, BMP-2-loaded scaffold (BMP-2), BMP-2 alginate microbeads (AM) with scaffold (BMP-2 AM), PDA-coated scaffold (BMP-2/PDA), and BMP-2 AM with PDA-coated scaffold (BMP-2 AM/PDA), were measured using ELISA over a 28-day period.

profile, with an initial BMP-2 release of approximately 31 % on day 1 and approximately 49 % on day 7, followed by sustained release for up to 28 days. The BMP-2 AM/PDA-coated scaffolds resulted in a slightly higher release of BMP-2, even after 7 days. The BMP-2/PDA scaffold group showed the lowest overall BMP-2 release rate of $26.77 \pm 0.10$ %. The initial burst was also the lowest among all groups, with $7.73 \pm 0.15$ % on day 1, $17.99 \pm 0.11$ % on day 7, and $20.81 \pm 0.17$ % on day 14. Moreover, a consistent BMP-2 release pattern at a rate of 3 % every 7 days was observed thereafter (Fig. 4B).

### 3.5. In vitro analysis of osteogenic potential in canine Ad-MSCs co-cultured with 3D-printed BMP-2-loaded AM scaffolds

Based on the release kinetics data, the osteogenic capacity of canine Ad-MSCs co-cultured with each scaffold was evaluated during a 14-day period when most of the BMP-2 was released. The ALP staining results

pertaining to the ALP activity showed that in comparison with that of the control group, the BMP-2-treated group exhibited higher levels of ALP-stained areas on days 7 and 14. Furthermore, the BMP-2 AM scaffolds showed a significantly higher proportion of ALP-stained regions compared with that of the BMP-2 scaffolds (Fig. 5A and B). A quantitative assessment of ARS staining was performed to compare the formation of mineralized nodules. The findings indicated that the BMP-2 AM group demonstrated the most intense staining, whereas the BMP-2 adsorbed group exhibited greater staining than that of the control group, although the presence or absence of the PDA coating did not show any significant difference (Fig. 5C). In the co-cultured cells, the mRNA expression levels of osteogenic markers were evaluated using real-time PCR. The results revealed a modest increase in the expression of COL1A1 in the scaffold group on day 7 and a significant increase in the BMP-2 AM group on day 14 (Fig. 5D). The mRNA expression of ALP, which indicates osteoblastic activity, was highest in the BMP-2 AM
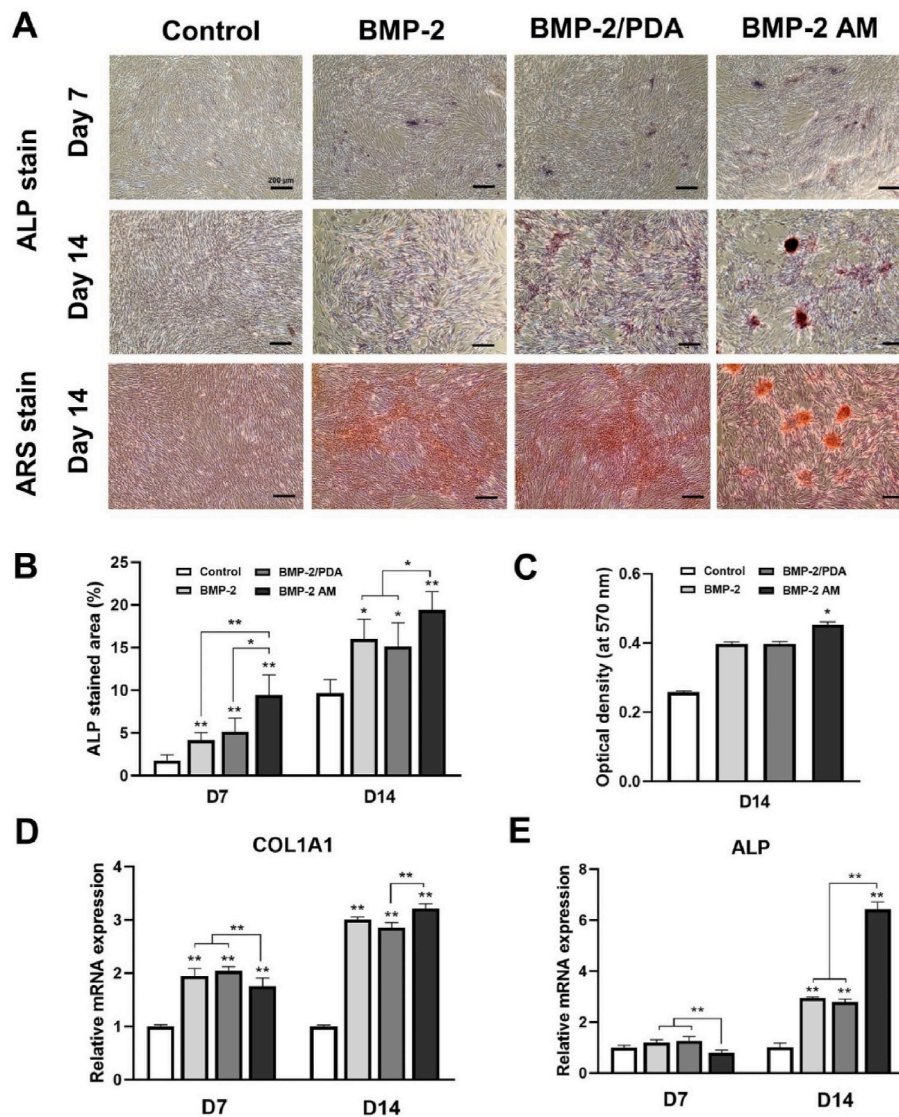
**Fig. 5. In vitro osteogenic differentiation of canine Ad-MSCs co-cultured with scaffold and alginate microbeads incorporating BMP-2** (A) ALP staining and ARS staining of canine Ad-MSCs co-cultured with each implant. Scale bar = 200 μm (B) Measured ALP-stained area on days 7 and 14 (C) ARS staining quantification on day 14 (D and E) The relative mRNA expression levels of osteogenic factors COL1A1 and ALP on days 7 and 14. Statistical significance was denoted using asterisks ($*p < 0.05$ and $**p < 0.01$).

group on day 14, whereas it was comparable among the BMP-2-adsorbed groups (Fig. 5E).

### 3.6. Postoperative monitoring and radiographic image analysis of rabbit femoral defects

Following implantation surgery using the aforementioned procedure (Supplementary Fig. 1), the condition of the rabbits was carefully monitored, and antibiotics and analgesics were administered as required. None of the animals experienced any postoperative complications such as pain response or surgical site infection, and all animals showed favourable vitality and appetite. To monitor the recovery of the surgical site, X-ray imaging was performed at 4-week intervals after mild sedation. On week 4, a slight increase in radiopacity was observed within the defect in the groups in which BMP-2 was applied, except for the group in which only the scaffold was implanted. From week 8 onward, bone union along the proximal or distal cortical bone was observed in some rabbits. On week 12, cortical bone formation and connectivity were observed along with bone remodelling; particularly, the BMP-2 AM/PDA and BMP-2/PDA groups exhibited a higher

radiological score of $9.00 \pm 0.81$ and $8.25 \pm 1.5$, respectively (Fig. 6).

### 3.7. Micro-CT analysis of bone growth in transplanted 3D-printed scaffolds

The distribution of bone growth within a 3D-printed scaffold implanted in a femoral segmental bone defect was investigated using micro-CT imaging of the transverse and sagittal cross-sections and 3D-reconstructed images (Fig. 7A). To determine the volume of new bone formation according to its location within the defect, the inside of the scaffold was designated as the Scaffold ROI and outside as the peripheral ROI (Fig. 7B). The quantity of bone growth within the scaffold was highest in the BMP-2 AM/PDA group, followed by the BMP-2/PDA, BMP-2 AM, BMP-2, and control groups; the level of bone growth was higher in the PDA-coated scaffold group than in the other groups (Fig. 7C). Bone formation within the peripheral ROI was similar in all groups except in the BMP-2 group, whereas the control group exhibited a higher bone volume within the peripheral ROI than that of the other groups owing to the formation of a massive bony callus in the periphery (Fig. 7D). The total ROI represents the overall amount of bone formation
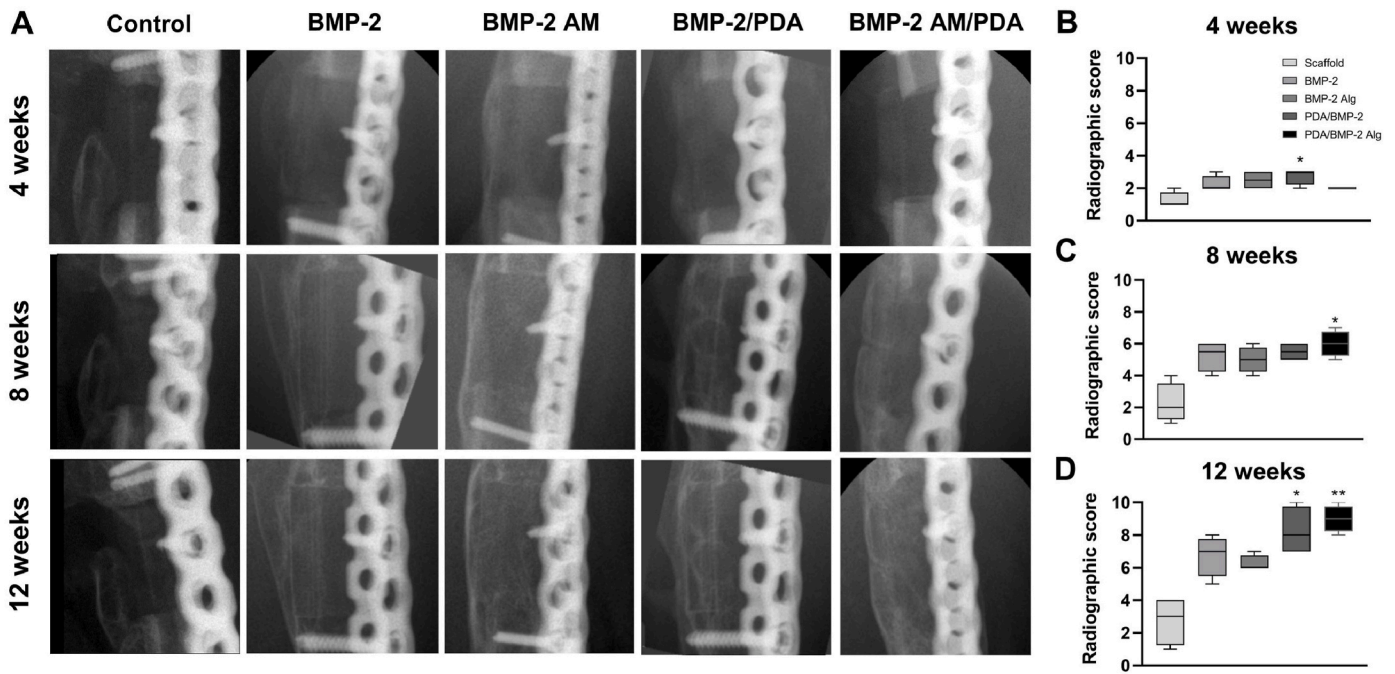
**Fig. 6. Radiographic images and scoring at 4, 8, and 12 weeks after surgery** (A) Caudocranial-view radiographic images of the femoral bone defect site were obtained at four-week intervals. Radiographic scores were analysed in all groups at 4 weeks (B), 8 weeks (C), and 12 weeks (D) after implantation. Statistical significance to scaffold group is indicated by asterisks (*$p < 0.05$, **$p < 0.01$).

in the defect, and both the BMP-2/PDA and BMP-2 AM/PDA groups showed a significant increase in bone formation compared with that of the BMP-2-adsorbed scaffold ($p < 0.05$) (Fig. 7E). The pMOI, which indicates the resistance to rotational motion, was higher in the BMP-2 AM, BMP-2/PDA, and BMP-2 AM/PDA groups than in the BMP-2 and control groups (Fig. 7F).

### 3.8. Histological analyses of bone growth pattern and connectivity within 3D-printed scaffolds

In the control group, fibrous tissue was found both inside and outside the scaffold along with callus formation on the scaffold's exterior and bone sclerosis at the bone–scaffold interface. The BMP-2 group presented slight ectopic ossification around the scaffold strands, although continuity of the newly formed bone was not confirmed. Furthermore, cyst-like bone formation occurred outside the scaffold. The BMP-2 AM group exhibited cortical bone continuity outward from the scaffold. However, scarce bone formation was observed within the scaffold strands, and microbeads were detected within the medullary cavity. Additionally, bone formation was observed around the microbeads. In contrast, the BMP-2/PDA group exhibited significant osteogenesis along the proximal and distal edges of the scaffold cortical region. The newly formed bone extended around the scaffold strands and displayed complete connectivity between the scaffold and the host bone. Similarly, the BMP-2 AM/PDA group showed considerable bone formation and connectivity including bone formation surrounding the beads in the medullary cavity (Fig. 8).

### 4. Discussion

Developing a synthetic bone implant that mimics the complex characteristics of natural bone is challenging. Integration of bioactivity, osteogenic promotion, mechanical properties, and scaffold architecture is essential for the successful design and fabrication of functional implants [24]. In this study, the osteogenic capacity of 3D-printed synthetic bone grafts composed of PCL/β-TCP scaffolds with or without PDA coating and BMP-2-loaded AM was assessed. These results showed that

PDA-coated PCL/β-TCP long bone substitutes with sustained BMP-2 delivery exhibited promising therapeutic effects against load-bearing bone defects in both in vitro assessments and an in vivo rabbit femoral segmental defect model.

Regarding the biocompatibility of the PCL/β-TCP scaffold and alginate microbeads, the CCK-8 assay results following co-culturing with canine Ad-MSCs revealed there were no statistically significant differences in cell viability between cells co-cultured with the scaffold materials and the control group of untreated cells. Nevertheless, similar trends in cell viability were observed, suggesting that the materials do not exhibit notable cytotoxicity. Additionally, serial radiographic and clinical observations conducted 12 weeks after surgery did not reveal any indications of inflammation, such as swelling, pain, or fever [25]. Furthermore, the efficacy of the scaffold and alginate microbeads as BMP-2 delivery carriers was confirmed by analysing the release pattern and comparing the mRNA expression levels after in vitro co-culture. The ELISA results showed that the uncoated scaffold exhibited an initial surge in BMP-2 release, whereas the PDA-coated scaffold displayed a more stable and sequential BMP-2 release for 28 days. These findings provide evidence that the PDA coating efficiently immobilizes BMP-2 onto scaffold surfaces, in agreement with previous studies [16,26]. However, the in vitro bioactivity of the released BMP-2 was similar in both scaffold groups, as indicated by similar levels of ALP activity, mineralization, and RT-qPCR expression. Notably, the BMP-2 AM group exhibited the highest ALP activity, mineralization, and osteogenic gene expression. This could be attributed to the similar release pattern of BMP-2 observed in the BMP-2 adsorbed groups following the initial burst until day 3. In contrast, the BMP-2 AM group showed a relatively higher release from days 3–14. These findings are in accordance with prior research, suggesting that the biological effects of BMP-2 on MSC differentiation and mineralization occur during the late phase of MSC culture, specifically from days 7–14 [27]. Based on these in vitro findings, the developed scaffolds and AMs were found to be biocompatible and function effectively as bioactive BMP-2 delivery vehicles, particularly in the case of BMP-2 AM.

The design of the developed 3D-printed scaffold, which mimics the anatomical structure of rabbit femurs, featured a macroporous
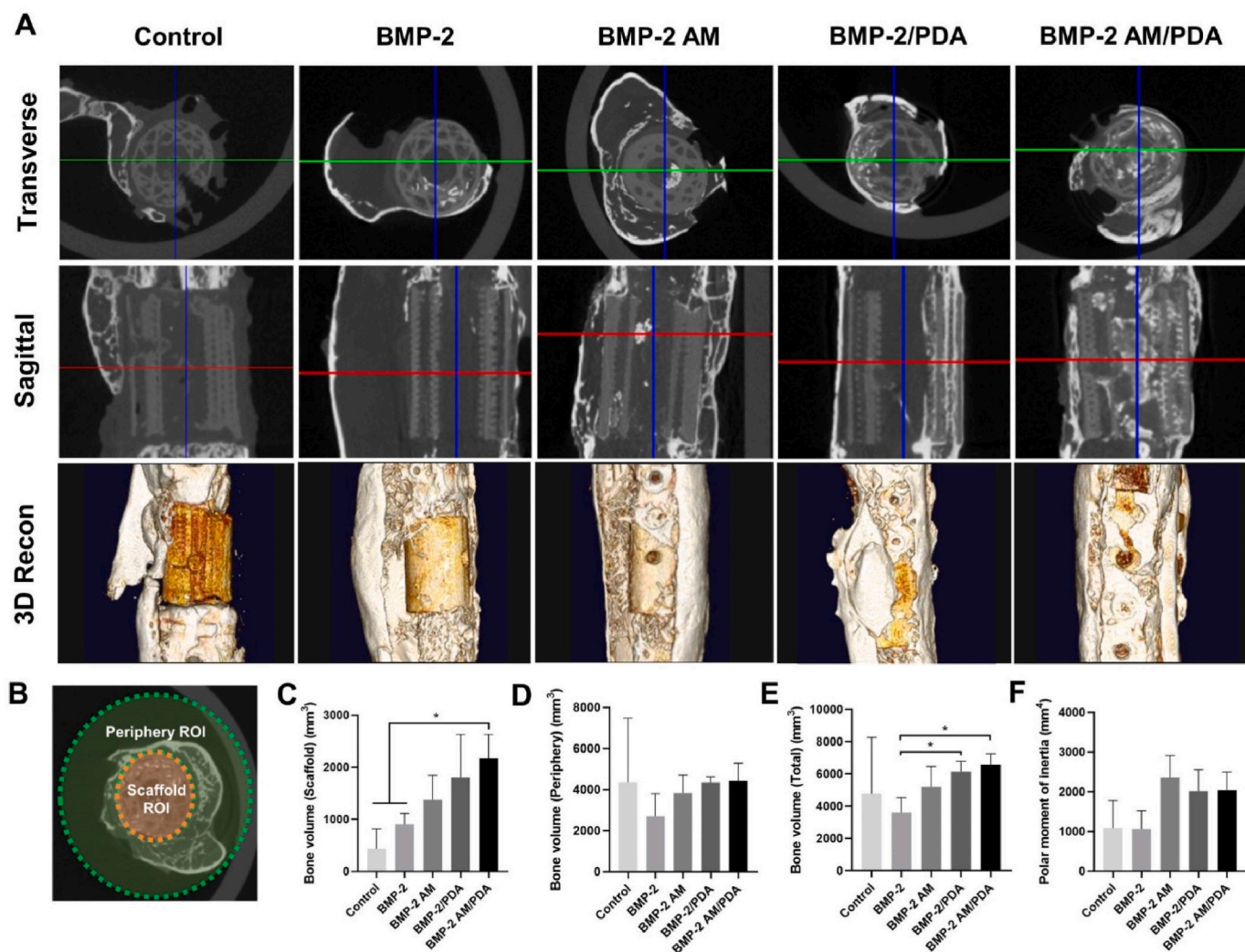
**Fig. 7. Microcomputed tomography (microCT) images and analysis of newly formed bone within bone defect at week 12** (A) Transverse, sagittal, and 3D-reconstructed images of the bone defect region (B) A region of interest (ROI) was selected inside the scaffold (Scaffold ROI) and outside the scaffold (Periphery ROI). The scaffold bone volume (C), peripheral bone volume (D), total bone volume (E), and polar moment of inertia (F) were measured for all groups. Statistical significance is indicated by asterisks (*$p < 0.05$).

interconnected cortical region and a hollow cancellous region. All implanted 3D-printed scaffolds remained well-stabilized with the host bone without major complications for 12 weeks. This favourable outcome can be attributed to scaffold design and the use of a stable fixation method. Particularly, the cortical region of the scaffold provides a broad bone-implant interface, ensuring robust mechanical engagement [28]. Additionally, certain groups treated with BMP-2 showed notable bone regeneration along both the outer and inner surfaces of the cortical region of the scaffold. This observation confirms the positive effects of additional mechanical support and planned osseointegration. With regard to the fixation methods, locking plates were applied in two sizes in the craniolateral and caudolateral directions using an orthogonal plating technique to minimize the instability and potential failure of the bone scaffold. This approach was also expected to maximize the screw purchase in the triangular-shaped rabbit bone model. Moreover, the orthogonal application of locking plates provides sufficient load-bearing effects, which provides efficient resistance to axial and torsional loading when treating long bone fractures in clinical environments [29]. Therefore, the developed 3D printed scaffold and orthogonal plating created a stable biological environment capable of inducing bone formation. The scaffold design was suitable for promoting bone regeneration in a manner similar to that of the natural bone structure.

For the successful clinical application of the scaffold, it needs to serve as a bridge between bone fragments, promoting connectivity by inducing bone regeneration inside and outside the scaffold [30,31]. The scaffold used in this study had a solid barrier that was designed to prevent fibrous tissue growth from the adjacent soft tissue; hence, internal osteoinduction was necessary. When this fabricated bone substitute was implanted into rabbit femoral shaft defects, the control group with only the scaffold application showed histological evidence of bone sclerosis at the bone interface and the presence of a hypertrophic callus, indicating instability and a lack of biological cues between the scaffold and bone fragments [32]. In the BMP-2 adsorption groups, the release kinetics results suggested that the initial high amount of BMP-2 released may have contributed to the formation of cystic bone instead of bone formation along the scaffold. This finding aligns with those of previous studies, indicating that higher doses of BMP-2 can upregulate adipogenesis and osteoclastogenesis, potentially leading to excessive bone resorption [20]. In contrast, the BMP-2 AM group with an uncoated scaffold exhibited a tendency for higher internal bone volume than in did the BMP-2-adsorbed group. This also corresponds with the ELISA and in vitro co-culture study findings, which revealed prolonged BMP-2 release and elevated expression of COL1A1 and ALP genes in the BMP-2
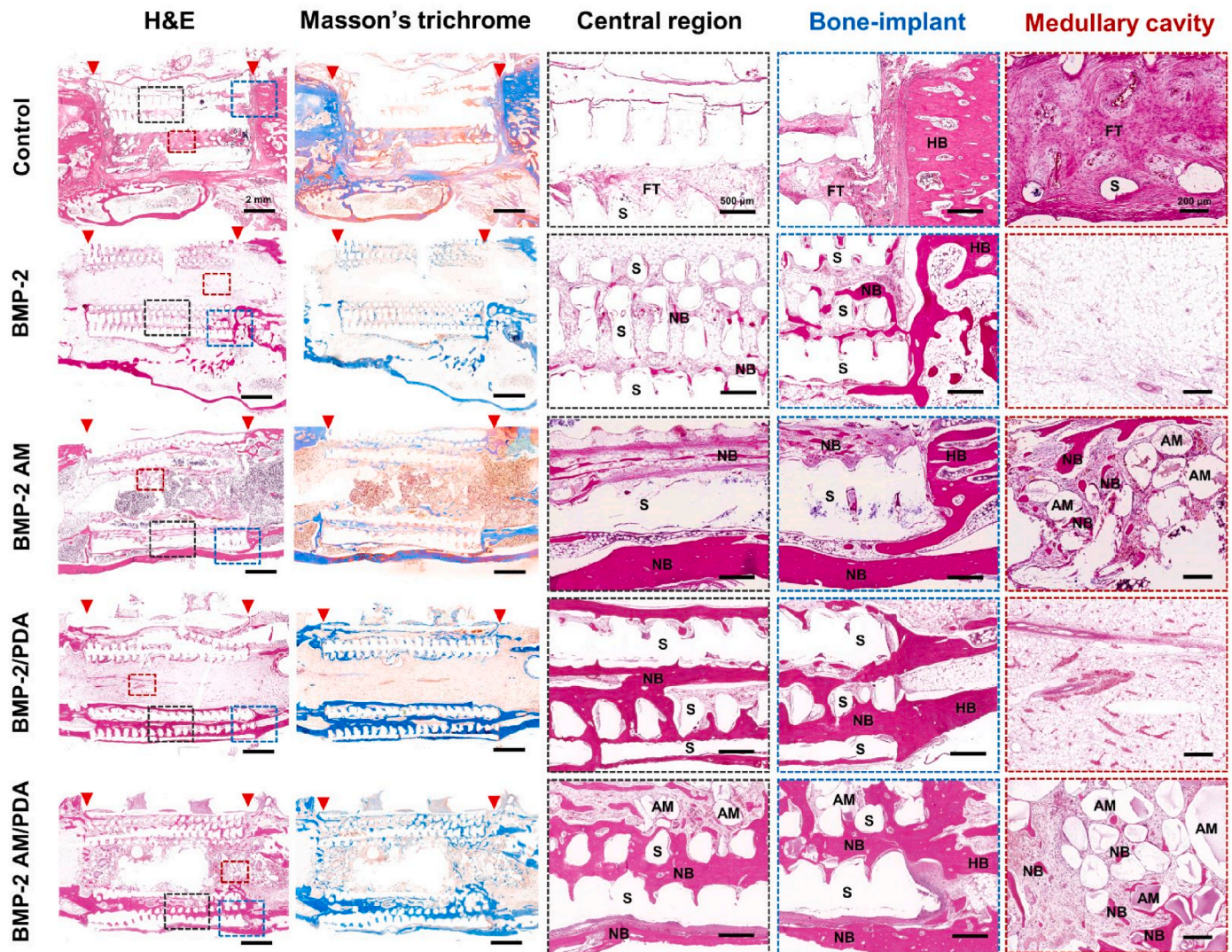
**Fig. 8. Histological sections of *in vivo* bone regeneration at 12 weeks after implantation.** Hematoxylin–eosin (H&E) and Masson's trichrome staining of regenerated bone within defects. Red arrows indicate the proximal and distal borders of the scaffold. Scale bar = 2 mm. The centre portion, bone-implant interface, and medullary cavity region of the implanted scaffold are magnified in black, blue, and red dotted box, respectively. Scale bar = 500 μm for the black and blue boxes) and 200 μm for the red box. AM: alginate microbeads; FT: fibrous tissue; HB: host bone; NB: newly formed bone; S: scaffold. (For interpretation of the references to color in this figure legend, the reader is referred to the Web version of this article.)

AM group. Additionally, ectopic bone formation and vascularization surrounding the BMP-2 microbeads located within the medullary canal further supported the occurrence of internal bone regeneration [33]. Thus, the use of BMP-2 AM proved to be a more efficient approach for achieving spatiotemporal osteoinduction within a scaffold compared with the BMP-2 adsorption technique.

Following PDA coating, the surface wettability of the PCL/β-TCP scaffold markedly improved, indicating enhanced hydrophilicity compared with that of the uncoated scaffold. This increase in hydrophilicity is directly correlated with the PDA concentration, leading to enhanced cell adhesion. Additionally, the presence of catechol and quinone groups in PDA facilitated the covalent attachment of BMP-2 to its amino side chains [34]. The distinct release pattern in the PDA-coated scaffold group indicates that the results of this study indirectly suggest stronger immobilization of BMP-2. The BMP-2 adsorbed onto the scaffold surface can then actively participate in the proliferation and differentiation of attached cells, promoting new bone formation [12,34]. Consequently, an increase in the new bone volume within the scaffold was observed in both groups with PDA-coated scaffolds, regardless of the BMP-2 delivery method. Although this finding differs from that of

the in vitro co-culture results, the lower amounts of BMP-2 released both initially and over time in the BMP-2 adsorbed PDA-coated scaffold group are speculated to have contributed to outcomes that were distinct between the short-term changes at the cellular level and the long-term effects over three months. Therefore, the PDA coating facilitates osseointegration into the 3D-printed scaffold by promoting cell and growth factor attachment and inducing direct contact between osteogenic cells and implant surfaces, ultimately resulting in new bone formation [35].

The ultimate goal of bone tissue engineering is to replace the scaffold with newly formed bone tissue as the scaffold gradually degrades while facilitating bone formation [36]. The PCL/β-TCP scaffold fabricated in this study was composed of PCL and β-TCP in an 8:2 ratio to establish a balance between ease of 3D printing and enhanced osteoconductive ability of the scaffold. Degradation rates can vary depending on various factors; in general, PCL has a degradation period of approximately 3–4 years in the body, whereas β-TCP undergoes 90 % degradation within a year. Therefore, the PCL/TCP scaffold degrades faster compared with PCL alone, and previous studies have reported approximately 33 % degradation of the PCL/β-TCP scaffold within 6–9 months following in

vivo application [37,38]. Furthermore, surface modifications can increase the hydrophilicity of a scaffold, leading to increased water uptake and accelerated hydrolysis, thereby promoting faster degradation. Hence, the application of PDA coatings can accelerate the degradation of 3D printed scaffolds [39]. Furthermore, previous studies have suggested that within a biological environment, the divalent cations such as $Ca^{2+}$ that constitute the alginate beads in simultaneously applied alginate microbeads are gradually replaced by monovalent cations such as $Na^+$ present in the surrounding tissues. This process induces the partial oxidation of alginate, resulting in its transformation into a water-soluble state [40]. In this study, the degradation of some alginate microbeads, accompanied by the formation of surrounding bone tissue encapsulating them, was also observed. Although further long-term degradation studies are needed, the findings of this study provide evidence of favourable osteoconductivity and biodegradability of the implanted materials for long-term bone defect healing.

## 5. Conclusion

In this study, biocompatible 3D-printed PCL/β-TCP scaffolds and AMs for bone regeneration were initially fabricated. Subsequently, the application of the PDA coating onto the PCL/β-TCP scaffold significantly increased the observed cell adhesion and hydrophilicity of the scaffold compared with that of the uncoated scaffold, leading to enhanced BMP-2 immobilization and bone formation along the scaffold. Moreover, BMP-2 AM served as an efficient carrier for facilitating sustained release of BMP-2, thereby promoting bone formation within the scaffold. Consequently, these findings suggest that a PDA-coated 3D-printed PCL/β-TCP scaffold with prolonged delivery of BMP-2 could be a promising therapeutic option for addressing long bone segmental defects.

## Funding

## Authorship

S.L. and B.-J.K. conceived and designed the study. S.L., J.-H.K., Y.-H. K., J.H., and W.K.K. acquired the data. S.L., J.-H.K., and Y.-H.K. analyzed and interpreted the data. S.L. and J.-H.K. drafted the manuscript. S.J. and B.-J.K. critically revised it for important intellectual content. All authors approved the final version of the manuscript.

## Declaration of competing interest

The author(s) have no conflicts of interest relevant to this article.

## Appendix A. Supplementary data

Supplementary data to this article can be found online at https://doi.org/10.1016/j.jot.2024.08.013.

## References

[1] Henkel J, Woodruff MA, Epari DR, Steck R, Glatt V, Dickinson IC, et al. Bone regeneration based on tissue engineering conceptions—a 21st century perspective. Bone research 2013;1(1):216–48.

[2] Pederson WC, Person DW. Long bone reconstruction with vascularized bone grafts. Orthopedic Clinics 2007;38(1):23–35.

[3] Zhang Q, Zhang W, Zhang Z, Zhang L, Chen H, Hao M, et al. Femoral nonunion with segmental bone defect treated by distraction osteogenesis with monolateral external fixation. J Orthop Surg Res 2017;12(1):1–7.

[4] Masquelet A, Kanakaris NK, Obert L, Stafford P, Giannoudis PV. Bone repair using the Masquelet technique. JBJS 2019;101(11):1024–36.

[5] Bose S, Roy M, Bandyopadhyay A. Recent advances in bone tissue engineering scaffolds. Trends Biotechnol 2012;30(10):546–54.

[6] Bose S, Vahabzadeh S, Bandyopadhyay A. Bone tissue engineering using 3D printing. Mater Today 2013;16(12):496–504.

[7] Dwivedi R, Kumar S, Pandey R, Mahajan A, Nandana D, Katti DS, et al. Polycaprolactone as biomaterial for bone scaffolds: review of literature. Journal of oral biology and craniofacial research 2020;10(1):381–8.

[8] Liu B, Lun Dx. Current application of β-tricalcium phosphate composites in orthopaedics. Orthopaedic surgery 2012;4(3):139–44.

[9] Sa M-W, Kim JY. Fabrication and characteristic evaluation of three-dimensional blended PCL (60 wt%)/β-TCP (40 wt%) scaffold. Transactions of the Korean Society of Mechanical Engineers A 2014;38(4):371–7.

[10] Kazimierczak P, Przekora A. Osteoconductive and osteoinductive surface modifications of biomaterials for bone regeneration: a concise review. Coatings 2020;10(10):971.

[11] Lee H, Dellatore SM, Miller WM, Messersmith PB. Mussel-inspired surface chemistry for multifunctional coatings. science 2007;318(5849):426–30.

[12] Ko E, Yang K, Shin J, Cho S-W. Polydopamine-assisted osteoinductive peptide immobilization of polymer scaffolds for enhanced bone regeneration by human adipose-derived stem cells. Biomacromolecules 2013;14(9):3202–13.

[13] Lee H, Rho J, Messersmith PB. Facile conjugation of biomolecules onto surfaces via mussel adhesive protein inspired coatings. Adv Mater 2009;21(4):431–4.

[14] Xi Z-Y, Xu Y-Y, Zhu L-P, Wang Y, Zhu B-K. A facile method of surface modification for hydrophobic polymer membranes based on the adhesive behavior of poly (DOPA) and poly (dopamine). J Membr Sci 2009;327(1–2):244–53.

[15] Xu Y, Li H, Wu J, Yang Q, Jiang D, Qiao B. Polydopamine-induced hydroxyapatite coating facilitates hydroxyapatite/polyamide 66 implant osteogenesis: an in vitro and in vivo evaluation. Int J Nanomed 2018:8179–93.

[16] Zhang J, Li J, Jia G, Jiang Y, Liu Q, Yang X, et al. Improving osteogenesis of PLGA/HA porous scaffolds based on dual delivery of BMP-2 and IGF-1 via a polydopamine coating. RSC Adv 2017;7(89):56732–42.

[17] Li L, Li Y, Yang L, Yu F, Zhang K, Jin J, et al. Polydopamine coating promotes early osteogenesis in 3D printing porous Ti6Al4V scaffolds. Ann Transl Med 2019;7(11).

[18] Bessa PC, Casal M, Reis R. Bone morphogenetic proteins in tissue engineering: the road from laboratory to clinic, part II (BMP delivery). Journal of tissue engineering and regenerative medicine 2008;2(2-3):81–96.

[19] Haidar ZS, Hamdy RC, Tabrizian M. Delivery of recombinant bone morphogenetic proteins for bone regeneration and repair. Part B: delivery systems for BMPs in orthopaedic and craniofacial tissue engineering. Biotechnol Lett 2009;31:1825–35.

[20] Zara JN, Siu RK, Zhang X, Shen J, Ngo R, Lee M, et al. High doses of bone morphogenetic protein 2 induce structurally abnormal bone and inflammation in vivo. Tissue Eng 2011;17(9–10):1389–99.

[21] Lee KY, Mooney DJ. Alginate: properties and biomedical applications. Prog Polym Sci 2012;37(1):106–26.

[22] Lee YH, Lee BW, Jung YC, Yoon BI, Woo HM, Kang BJ. Application of alginate microbeads as a carrier of bone morphogenetic protein-2 for bone regeneration. J Biomed Mater Res B Appl Biomater 2019;107(2):286–94.

[23] Kim J, Lee S, Choi Y, Choi J, Kang B-J. Sustained release of bone morphogenetic protein-2 through alginate microbeads enhances bone regeneration in rabbit tibial metaphyseal defect model. Materials 2021;14(10):2600.

[24] Polo-Corrales L, Latorre-Esteves M, Ramirez-Vick JE. Scaffold design for bone regeneration. J Nanosci Nanotechnol 2014;14(1):15–56.

[25] Tian B, Wang N, Jiang Q, Tian L, Hu L, Zhang Z. The immunogenic reaction and bone defect repair function of ε-poly-L-lysine (EPL)-coated nanoscale PCL/HA scaffold in rabbit calvarial bone defect. J Mater Sci Mater Med 2021;32(6):63.

[26] Kim SE, Yun Y-P, Han Y-K, Lee D-W, Ohe J-Y, Lee B-S, et al. Osteogenesis induction of periodontal ligament cells onto bone morphogenic protein-2 immobilized PCL fibers. Carbohydr Polym 2014;99:700–9.

[27] Bai Y, Li P, Yin G, Huang Z, Liao X, Chen X, et al. BMP-2, VEGF and bFGF synergistically promote the osteogenic differentiation of rat bone marrow-derived mesenchymal stem cells. Biotechnol Lett 2013;35:301–8.

[28] Kittur N, Oak R, Dekate D, Jadhav S, Dhatrak P. Dental implant stability and its measurements to improve osseointegration at the bone-implant interface: a review. Mater Today Proc 2021;43:1064–70.

[29] El Beaino M, Morris RP, Lindsey RW, Gugala Z. Biomechanical evaluation of dual plate configurations for femoral shaft fracture fixation. BioMed Res Int 2019;2019.

[30] Suba Z, Takács D, Gyulai-Gaál S, Kovács K. Facilitation of β-tricalcium phosphate-induced alveolar bone regeneration by Platelet-Rich plasma in Beagle Dogs: a histologic and Histomorphometric study. Int J Oral Maxillofac Implants 2004;19(6).

[31] Liu Y, Luo D, Wang T. Hierarchical structures of bone and bioinspired bone tissue engineering. Small 2016;12(34):4611–32.

[32] Rupp M, Biehl C, Budak M, Thormann U, Heiss C, Alt V. Diaphyseal long bone nonunions—types, aetiology, economics, and treatment recommendations. Int Orthop 2018;42:247–58.

[33] Pearson HB, Mason DE, Kegelman CD, Zhao L, Dawahare JH, Kacena MA, et al. Effects of bone morphogenetic protein-2 on neovascularization during large bone defect regeneration. Tissue Eng 2019;25(23–24):1623–34.

[34] Kang Z, Li D, Shu C, Du J, Yu B, Qian Z, et al. Polydopamine coating-mediated immobilization of BMP-2 on polyethylene terephthalate-based artificial ligaments for enhanced bioactivity. Front Bioeng Biotechnol 2021;9:749221.

[35] Simon Z, Watson PA. Biomimetic dental implants-new ways to enhance osseointegration. J Can Dent Assoc 2002;68(5):286–9.

[36] Tajvar S, Hadjizadeh A, Samandari SS. Scaffold degradation in bone tissue engineering: an overview. Int Biodeterior Biodegrad 2023;180:105599.

[37] Lam CX, Hutmacher DW, Schantz JT, Woodruff MA, Teoh SH. Evaluation of polycaprolactone scaffold degradation for 6 months in vitro and in vivo. J Biomed Mater Res Part A: An Official Journal of The Society for Biomaterials, The Japanese Society for Biomaterials, and The Australian Society for Biomaterials and the Korean Society for Biomaterials 2009;90(3):906–19.

[38] Woodruff MA, Hutmacher DW. The return of a forgotten polymer—polycaprolactone in the 21st century. Prog Polym Sci 2010;35(10): 1217–56.

[39] Zhang H, Zhou L, Zhang W. Control of scaffold degradation in tissue engineering: a review. Tissue Eng B Rev 2014;20(5):492–502.

[40] Sahoo DR, Biswal T. Alginate and its application to tissue engineering. SN Appl Sci 2021;3(1):30.